

Layer Hall effect in a 2D topological axion antiferromagnet

<https://doi.org/10.1038/s41586-021-03679-w>

Received: 21 December 2020

Accepted: 27 May 2021

Published online: 21 July 2021

 Check for updates

Anyuan Gao¹, Yu-Fei Liu¹, Chaowei Hu², Jian-Xiang Qiu¹, Christian Tzschaschel¹, Barun Ghosh^{3,4}, Sheng-Chin Ho¹, Damien Bérubé¹, Rui Chen⁵, Haipeng Sun⁵, Zhaowei Zhang⁶, Xin-Yue Zhang⁷, Yu-Xuan Wang⁷, Naizhou Wang⁶, Zumeng Huang⁶, Claudia Felser⁸, Amit Agarwal³, Thomas Ding⁷, Hung-Ju Tien⁹, Austin Akey¹⁰, Jules Gardener¹⁰, Bahadur Singh¹¹, Kenji Watanabe¹², Takashi Taniguchi¹³, Kenneth S. Burch⁷, David C. Bell^{10,14}, Brian B. Zhou⁷, Weibo Gao⁶, Hai-Zhou Lu⁵, Arun Bansil⁴, Hsin Lin¹⁵, Tay-Rong Chang^{9,16,17}, Liang Fu¹⁸, Qiong Ma⁷, Ni Ni¹²✉ & Su-Yang Xu¹✉

Whereas ferromagnets have been known and used for millennia, antiferromagnets were only discovered in the 1930s¹. At large scale, because of the absence of global magnetization, antiferromagnets may seem to behave like any non-magnetic material. At the microscopic level, however, the opposite alignment of spins forms a rich internal structure. In topological antiferromagnets, this internal structure leads to the possibility that the property known as the Berry phase can acquire distinct spatial textures^{2,3}. Here we study this possibility in an antiferromagnetic axion insulator—even-layered, two-dimensional MnBi_2Te_4 —in which spatial degrees of freedom correspond to different layers. We observe a type of Hall effect—the layer Hall effect—in which electrons from the top and bottom layers spontaneously deflect in opposite directions. Specifically, under zero electric field, even-layered MnBi_2Te_4 shows no anomalous Hall effect. However, applying an electric field leads to the emergence of a large, layer-polarized anomalous Hall effect of about $0.5e^2/h$ (where e is the electron charge and h is Planck's constant). This layer Hall effect uncovers an unusual layer-locked Berry curvature, which serves to characterize the axion insulator state. Moreover, we find that the layer-locked Berry curvature can be manipulated by the axion field formed from the dot product of the electric and magnetic field vectors. Our results offer new pathways to detect and manipulate the internal spatial structure of fully compensated topological antiferromagnets^{4–9}. The layer-locked Berry curvature represents a first step towards spatial engineering of the Berry phase through effects such as layer-specific moiré potential.

Ever since the first use of lodestone for navigation, magnetism has played a central role in fundamental research and technology developments. As we enter the quantum era, an important goal of modern condensed matter is to search for quantum magnets, where effects such as electronic correlations, symmetry breaking and the Berry phase interact with magnetism, leading to exotic phenomena that do not exist in conventional magnetic materials. Antiferromagnetism is an elementary yet fascinating type of magnetic order. Antiferromagnets are internally magnetic, but their zero net magnetization makes the magnetism externally invisible. Studies of the internal structures of

quantum antiferromagnets have led to breakthroughs such as Mott insulators, high-critical-temperature superconductors, magnetoelectrics and antiferromagnetic spintronics^{10,11}.

Compared with its important role in the areas above, antiferromagnetism has not featured prominently in the field of topological materials. However, recent theoretical work^{2,3,9,12–20} has increasingly recognized this exciting prospect. Many topological phenomena that arise from the interplay between antiferromagnetism and topology have been proposed, including the condensed matter realization of axions (a dark matter candidate)²¹, the generation of dissipationless spin current in the absence

¹Department of Chemistry and Chemical Biology, Harvard University, Cambridge, MA, USA. ²Department of Physics and Astronomy and California NanoSystems Institute, University of California, Los Angeles, Los Angeles, CA, USA. ³Department of Physics, Indian Institute of Technology, Kanpur, India. ⁴Department of Physics, Northeastern University, Boston, MA, USA.

⁵Shenzhen Institute for Quantum Science and Engineering and Department of Physics, Southern University of Science and Technology (SUSTech), Shenzhen, China. ⁶Division of Physics and Applied Physics, School of Physical and Mathematical Sciences, Nanyang Technological University, Singapore, Singapore. ⁷Department of Physics, Boston College, Chestnut Hill, MA, USA.

⁸Max Planck Institute for Chemical Physics of Solids, Dresden, Germany. ⁹Department of Physics, National Cheng Kung University, Tainan, Taiwan. ¹⁰Center for Nanoscale Systems, Harvard University, Cambridge, MA, USA. ¹¹Department of Condensed Matter Physics and Materials Science, Tata Institute of Fundamental Research, Mumbai, India. ¹²Research Center for Functional Materials, National Institute for Materials Science, Tsukuba, Japan. ¹³International Center for Materials Nanoarchitectonics, National Institute for Materials Science, Tsukuba, Japan. ¹⁴Harvard John A. Paulson School of Engineering and Applied Sciences, Harvard University, Cambridge, MA, USA. ¹⁵Institute of Physics, Academia Sinica, Taipei, Taiwan. ¹⁶Center for Quantum Frontiers of Research and Technology (QFort), Tainan, Taiwan. ¹⁷Physics Division, National Taiwan University for Theoretical Sciences, National Taiwan University, Taipei, Taiwan. ¹⁸Department of Physics, Massachusetts Institute of Technology, Cambridge, MA, USA. ✉e-mail: suyangxu@fas.harvard.edu; nini@physics.ucla.edu

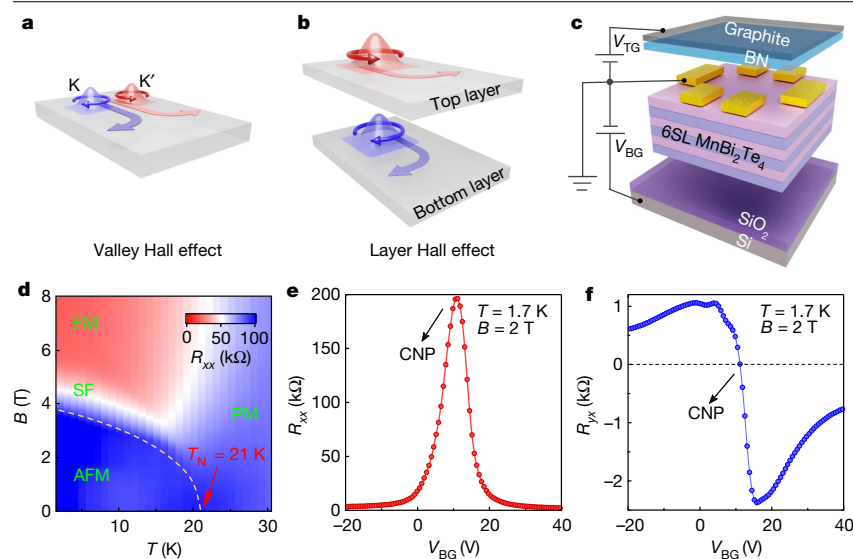


Fig. 1 | Basic characterizations of the antiferromagnetic six-SL MnBi₂Te₄. **a**, Illustration of the valley Hall effect. In certain non-magnetic quantum materials, such as gapped graphene and transition metal dichalcogenides, Berry curvature is locked to the K and K' valleys. Electrons in opposite valleys deflect in opposite directions, leading to the valley Hall effect. **b**, Illustration of the layer Hall effect. In the antiferromagnetic topological insulator state of even-layered MnBi₂Te₄, Berry curvature is locked to the top and bottom layers. Hence electrons in the top and bottom layers deflect in opposite directions, leading to the layer Hall effect. A bilayer system is shown for simplicity. **c**, Schematic drawing of our dual-gated devices. V_{BG} , bottom gate voltage; V_{TG} , top gate voltage. **d**, Longitudinal resistance R_{xx} as a function of temperature (T) and magnetic field (B). The magnetic states are indicated on the plot: AFM, antiferromagnetic; FM, ferromagnetic; SF, spin-flop; PM, permanent magnet. **e**, **f**, R_{xx} and R_{xy} as a function of V_{BG} in the antiferromagnetic phase at $B = 2$ T. CNP, charge-neutral point.

of a concomitant charge current¹⁴, and the presence of giant/quantized magneto-electric and magneto-optoelectronic couplings^{12,15,16,19,20}. Further integrating this new topological physics with spintronics could give rise to topological antiferromagnetic spintronics⁷, in which the storage, transportation and manipulation of magnetic data could become much faster, more robust and energy-efficient.

To experimentally fulfil this potential, important questions remain to be answered, including how topology and Berry curvature are encoded in antiferromagnets and how they can be controlled. As discussed above, the primary characteristic of an antiferromagnet is its internal structure. This raises intriguing possibilities beyond the spontaneous anomalous Hall effect (AHE) in ferromagnetic systems, which measures the total Berry curvature²². We can ask whether the topology and the Berry phase can acquire distinct spatial structures^{2,3} and whether such a spatially locked Berry phase will give rise to new kinds of Berry-curvature-induced Hall responses. Here we investigate these possibilities in even-layered MnBi₂Te₄ flakes.

In addition to charge, electrons can feature additional degrees of freedom such as spin, valley and layer. Encoding Berry curvature with these degrees of freedom can lead to new types of Hall effect. A primary example is the valley Hall effect (Fig. 1a), which has been realized in gapped graphene and transition metal dichalcogenides²³. The layer Hall effect studied here is a new phenomenon in which electrons from the top and bottom layers deflect in opposite directions (Fig. 1b).

MnBi₂Te₄ has recently attracted great interest^{24–33}, since it bridges the fields of topology, magnetism and two-dimensional (2D) van der Waals materials. The basic building block of the crystal is a septuple layer (SL), which consists of seven atomic layers in the sequence Te–Bi–Te–Mn–Te–Bi–Te. The lattice is built by stacking identical SLs separated by the van der Waals gap. Its magnetic ground state is an A-type antiferromagnet, in which Mn spins within each SL are ferromagnetically aligned along the z axis but Mn spins between adjacent SLs are antiparallel. Moreover, a magnetic field along the z axis can drive the antiferromagnet to a spin-flop phase (≥ 4 T) and then to a fully polarized ferromagnetic phase (≥ 8 T)^{26,27}. The magnetic and topological states of 2D MnBi₂Te₄ flakes can therefore be categorized into two types. The first kind is ferromagnetic or ferromagnetic-like, in which the 2D system has an unequal number of up-spin layers and down-spin layers and therefore features a global magnetization. These systems break the space-time \mathcal{PT} symmetry. In these ferromagnetic or ferromagnetic-like systems, pioneering work^{28–33} has reported large or quantized AHE. The second kind is the fully compensated antiferromagnet, in which the 2D system has an equal number of up-spin

layers and down-spin layers. These systems preserve \mathcal{PT} symmetry. Previous research^{29,34,35} has prepared systems in which the condition for this phase is expected to occur and observed a highly insulating behaviour with zero Hall conductivity. However, the topological and Berry phase properties of the axion insulator have not been directly probed.

Layer Hall effect

We have fabricated high-quality, dual-gated MnBi₂Te₄ devices (Fig. 1c). The overall magnetic behaviour shows the expected phase diagram (Fig. 1d). The magnetic-field-induced ferromagnetic state is found to be a topological Chern insulator, as demonstrated by the vanishing longitudinal resistance R_{xx} and fully (100%) quantized Hall resistance R_{xy} (Extended Data Fig. 2b–d).

We now focus on the antiferromagnetic ground state. The longitudinal resistance R_{xx} (Fig. 1e) as a function of the bottom gate voltage V_{BG} peaks sharply, signalling insulating behaviour at charge neutrality. The Hall resistance R_{xy} (Fig. 1f) also features a clear sign-reversal at charge neutrality. We further study the magnetic field dependence of R_{xy} . As shown in Fig. 2a, the data show the absence of spontaneous AHE, revealing a vanishing total Berry curvature in even-layered MnBi₂Te₄. As such, the transport measurements above do not show distinct evidence for non-trivial topology or Berry curvature in the antiferromagnetic phase of 6SL MnBi₂Te₄ (that is, six sets of septuple layers). In fact, the observed diverging resistance and vanishing AHE are common behaviours of any non-magnetic semiconductor. A new experimental tuning parameter is needed to uncover the rich Berry curvature properties in this antiferromagnetic topological system.

We now explore the electric-field dependence of the antiferromagnetic phase. In the presence of a finite electric field, we observe (Fig. 2b) that forward and backward scans become clearly separated in the antiferromagnetic phase, suggesting the emergence of a large AHE on application of the field. We now study how this AHE depends on electric field. Remarkably, we found (Fig. 2c) that the AHE flips sign as one reverses the direction of the electric field (see similar data in Extended Data Fig. 3a). This electric-field-reversible AHE represents a fundamental piece of evidence for the layer Hall effect.

We then study how the AHE depends on the charge density n . The AHE is found to show opposite sign depending on whether the system is electron-doped or hole-doped (Fig. 3a). At charge neutrality, the AHE vanishes. With a smaller electric field (Fig. 3b), we observe a similar dependence on n , although the overall magnitude of the AHE

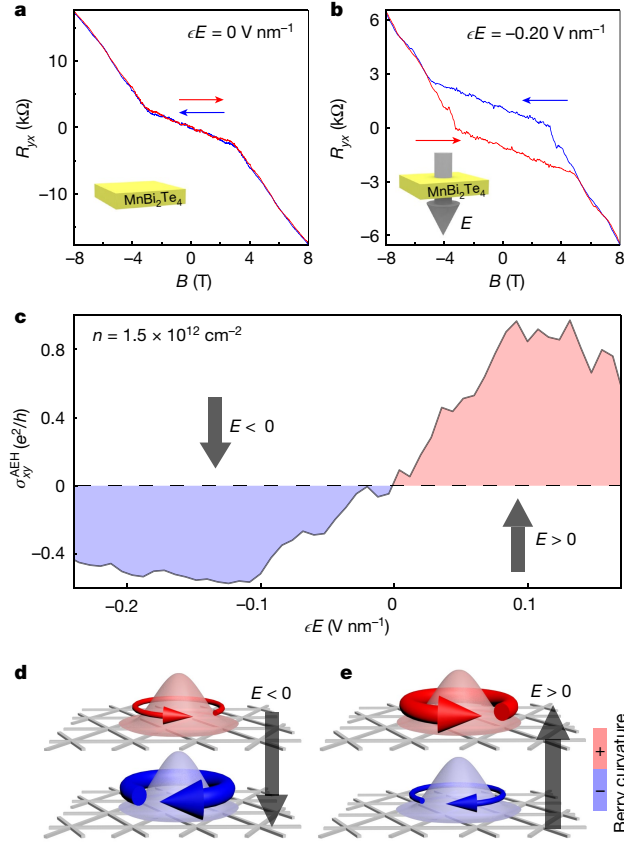


Fig. 2 | Observation of the layer Hall effect. **a**, R_{yx} as a function of B field at zero electric field. Red and blue curves denote the forward and backward scans, respectively. The $E = 0$ condition is determined by the maximum of the resistance R_{xx} (see Supplementary Information section V.2). **b**, Same as **a** but at a finite electric field $cE = -0.20 \text{ V nm}^{-1}$ (where ϵ is the permittivity of the sample), demonstrating the electric-field-induced AHE. **c**, The AHE conductivity (at $B = 0$) σ_{yx}^{AHE} as a function of electric field. The charge density n is set in the electron-doped regime ($n = +1.5 \times 10^{12} \text{ cm}^{-2}$). **d, e**, Illustration of the layer-locked Berry curvature under opposite electric fields. Depending on the electric-field direction, the Berry curvature contribution from a particular layer dominates. This explains the AHE's sign reversal with respect to electric field. The colour denotes the sign of the Berry curvature. The sizes of the rotating arrows denote the magnitude of the total Berry curvature from a particular layer. A bilayer system is illustrated for simplicity.

is reduced. In sharp contrast, for the ferromagnetic-like, odd-layered MnBi_2Te_4 , our data (Extended Data Fig. 8a, b) show that the AHE remains the same sign in the hole-doped and electron-doped regimes, consistent with previous results^{8,28,36}. The dependence on charge density of the electric-field-induced AHE in even-layered AFM MnBi_2Te_4 , combined with the distinctly different behaviour in odd-layered ferromagnetic-like systems, provides important insights into its microscopic origin.

We further study the temperature dependence of the AHE. As shown in Extended Data Fig. 4b, at $T = 2 \text{ K}$, the AHE is pronounced. As we increase the temperature to 14 K , the AHE persists but weakens. As we further increase the temperature to be above the Néel temperature ($T_N \approx 21 \text{ K}$), the AHE vanishes entirely. This temperature dependence demonstrates that the observed AHE is a unique response of the magnetically ordered state.

We analyse the observed electric-field-induced AHE from the symmetry point of view. It has been established that the AHE conductivity σ^{AHE} arises from the total Berry curvature integrated over all occupied states²²; that is, $\sigma^{\text{AHE}} = \int_{\text{occupied states}} \Omega$, where Ω is the Berry curvature.

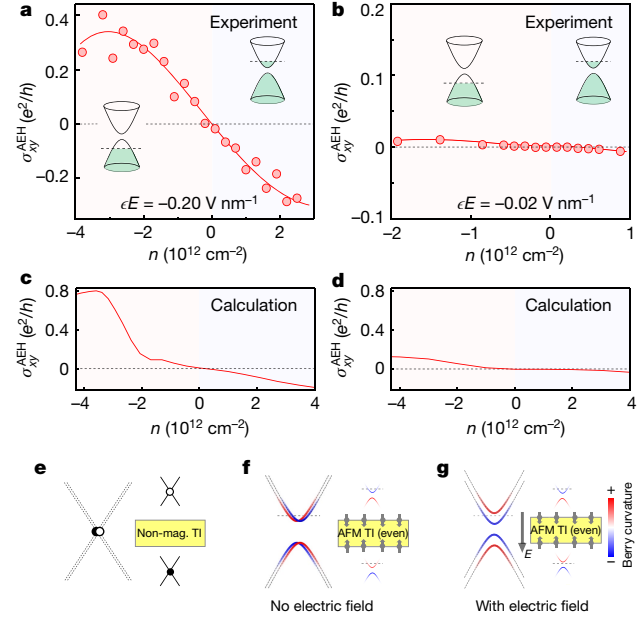


Fig. 3 | Charge-density dependence of the layer Hall effect and the layer-locked Berry curvature. **a, b**, The layer Hall effect as a function of charge density n with the electric field fixed at $cE = -0.20 \text{ V nm}^{-1}$ (**a**) and $cE = -0.02 \text{ V nm}^{-1}$ (**b**). **c, d**, First-principles calculated AHE conductivity σ_{yx}^{AHE} as a function of charge density. The theoretically applied electric field (E^{THY}) here can be related to the displacement field by $D^{\text{THY}} = \epsilon^{\text{MnBi}_2\text{Te}_4} E^{\text{THY}}$. **e–g**, A microscopic picture for the layer Hall effect in 6SL antiferromagnetic MnBi_2Te_4 . **e**, A non-magnetic topological insulator (TI) features massless surface Dirac fermions on its top and bottom layers. **f**, The inclusion of the A-type antiferromagnetic order gaps the Dirac fermions. The resulting Berry curvature of the top Dirac fermion exactly cancels that of the bottom Dirac fermion. **g**, Applying an electric field can break the degeneracy between the top and bottom Dirac fermions, leading to a large, layer-polarized AHE, as long as the Fermi level is away from the bandgap. This electric-field-induced AHE serves as the key evidence for the layer Hall effect and the layer-locked Berry curvature.

Importantly, both \mathcal{T} (time-reversal symmetry) and \mathcal{PT} (space-time symmetry) would force σ^{AHE} to vanish. Although all magnetic states break \mathcal{T} , what is intriguing about the antiferromagnetic state in even-layered MnBi_2Te_4 is that its internal spin structure preserves \mathcal{PT} . As a result: (1) in the absence of an electric field, the \mathcal{PT} symmetry forces the momentum-integrated Berry curvature and therefore the AHE to vanish; (2) the application of an electric field breaks \mathcal{PT} , which leads to the emergence of a finite AHE; and (3) because the electric field provides the critical \mathcal{PT} -breaking, flipping the electric field reverses the way in which \mathcal{PT} is broken, which, in turn, reverses the sign of the AHE. This symmetry analysis provides key evidence for the intrinsic nature (Methods; Supplementary Information sections III and IV).

Layer-locked Berry curvature

For insights beyond the global symmetry analysis, we now examine the microscopic mechanism. As a starting point, a non-magnetic topological insulator features massless Dirac fermions on its top and bottom surfaces (Fig. 3e). The inclusion of a magnetic order gaps these Dirac fermions, leading to giant Berry curvatures in each individual Dirac band (Fig. 3f). Owing to the combination of the A-type antiferromagnetic spin structure and the even number of layers, the top and bottom Dirac fermions experience opposite magnetizations and hence open up gaps in opposite fashion (Fig. 3f). As such, the Berry curvature contributed by the top Dirac fermion exactly cancels out that contributed by the bottom Dirac fermion, giving rise to a layer-locked

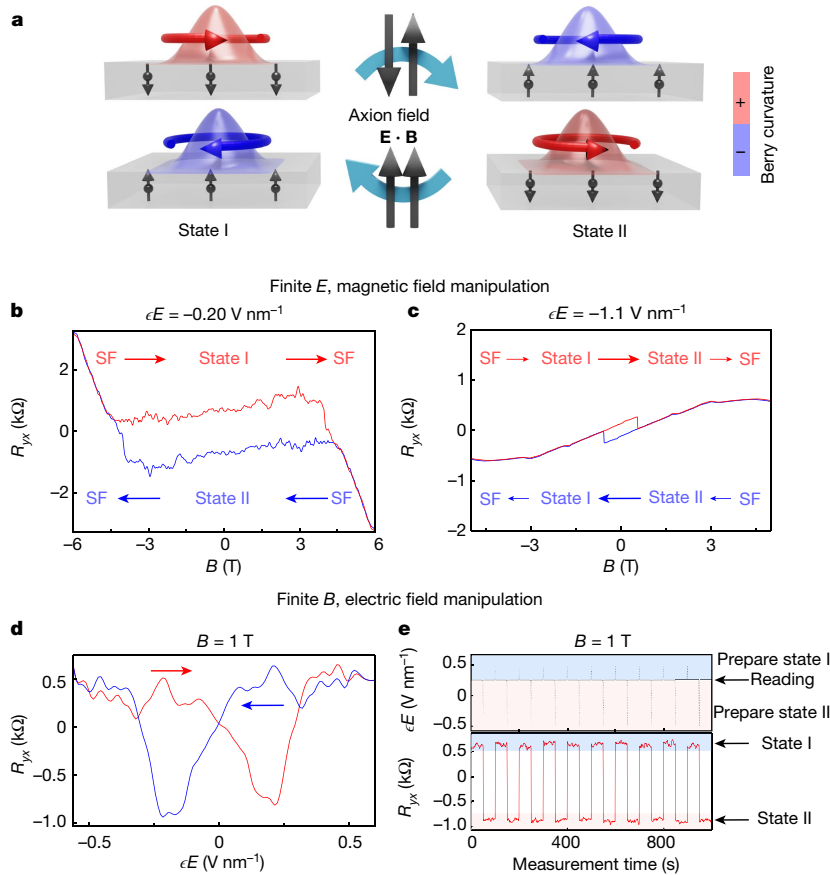


Fig. 4 | Manipulation of the layer-locked Berry curvature by the axion field $\mathbf{E} \cdot \mathbf{B}$ and electrical readout by the layer Hall effect. **a**, The axion field $\mathbf{E} \cdot \mathbf{B}$ (refs. ^{10,21,37}) can switch between the two antiferromagnetic states (states I and II), which, in turn, reverse the layer-locked Berry curvature. A bilayer system is illustrated for simplicity. **b**, R_{yx} versus the magnetic field B with $\epsilon E = -0.20 \text{ V nm}^{-1}$. **c**, Same as **b** but with $\epsilon E = -1.1 \text{ V nm}^{-1}$. **d**, R_{yx} versus E with $B = +1 \text{ T}$. **e**, Repeatable switching of the antiferromagnetic states using the electric field. The electric field sweeping is achieved by slow ramping of the gate voltage. The measurement time (horizontal axis) only counts the time at the targeted gate voltage. The sweeping time is not shown.

Berry curvature. Interestingly, the electric field can strongly break the degeneracy between top and bottom surfaces: $E > 0$ makes the contribution of the bottom layer dominant, whereas $E < 0$ makes the contribution of the top layer dominant. In other words, the direction of the electric field allows us to selectively probe the contribution from one layer over the other.

We now further study the dependence on the charge density n . Note that the Berry curvature of the lowest conduction band and that of the highest valence band are of the same sign in our cases (Fig. 3g, Extended Data Fig. 5). Therefore, going from charge neutrality to the electron-doped regime, we add a certain Ω ; going from charge neutrality to the hole-doped regime, we remove the same Ω . Consequently, under the same electric field, the AHE in the electron-doped regime and in the hole-doped regime has opposite sign, which is consistent with our experimental observations in Fig. 3a, b. We highlight that the sign-reversal with n is a unique signature of the layer Hall effect in the \mathcal{PT} -symmetric antiferromagnetic topological insulator. By contrast, in ferromagnetic or ferromagnetic-like systems, the conduction and valence bands have opposite Ω (Extended Data Fig. 8), which naturally explains why the AHE has the same sign in both electron-doped and hole-doped regimes.

We now directly compute the band structure, Berry curvature and σ^{AHE} of 6SL MnBi₂Te₄ using first-principles calculations. As shown in Fig. 3c, d, and in Extended Data Figs. 3c, d and 6, our first-principles calculations display good agreement with our experimental data in key aspects including the overall magnitude of the σ^{AHE} and the sign-reversal of σ^{AHE} with respect to E and n .

Overall, our measurements with dual-gated devices provide a large parameter space, which allows us to compare them with theoretical analysis and calculations. The electric-field-reversible AHE, taken

together with the layer selectivity of the electric field, provides strong evidence for the layer Hall effect and the layer-locked Berry curvature in MnBi₂Te₄. Notably, the layer Hall effect is already present at $E = 0$, although it only manifests itself upon application of the electric field.

Axion field manipulation

We now show that the layer-locked Berry curvature can be switched by driving the system between the opposite antiferromagnetic states (Fig. 4a). In ferromagnets, it is well known that magnetization can be switched by a magnetic field, and similarly, in ferroelectrics, electric polarization can be switched by an electric field. Interestingly, in our \mathcal{PT} -symmetric antiferromagnetic axion insulator system, neither a magnetic nor an electric field alone can accomplish the switching. Rather, Maxwell's equations in MnBi₂Te₄ are expected to be strongly modified, with a new axion field term $\Delta L = \theta \frac{e^2}{2\pi h c} \mathbf{E} \cdot \mathbf{B}$ (where c is the speed of light and θ is the axion angle)^{16,21} added to the Lagrangian (L) of electrodynamics. As a result, the antiferromagnetic order in the axion insulator state is expected to couple strongly to the axion $\mathbf{E} \cdot \mathbf{B}$ field^{10,21,37,38}.

To verify the manipulation by the axion field $\mathbf{E} \cdot \mathbf{B}$, we now examine the hysteresis observed in our data for R_{yx} versus B (for example, Fig. 4b) focusing on the two antiferromagnetic states. We first study the forward scan (red curve) in Fig. 4b. At $B \approx -4 \text{ T}$, the system changes from the spin-flop phase to the antiferromagnetic phase. Because a constant, negative electric field is applied in Fig. 4b, at $B \approx -4 \text{ T}$ the system enters the antiferromagnetic phase with a positive $\mathbf{E} \cdot \mathbf{B}$ field ($E < 0$ and $B < 0$). This $\mathbf{E} \cdot \mathbf{B}$ field can favour one antiferromagnetic state over the other. Similarly, for the backward scan (blue curve), the system changes from the spin-flop phase to the antiferromagnetic phase at $B \approx +4 \text{ T}$ with a negative $\mathbf{E} \cdot \mathbf{B}$, which favours the opposite antiferromagnetic state.

Therefore, owing to the finite $\mathbf{E} \cdot \mathbf{B}$, the system transits from the spin-flop phase to a particular antiferromagnetic state.

We continue to discuss Fig. 4b. As described above, in the forward scan, the system enters the antiferromagnetic state I at $B \approx -4$ T due to a positive $\mathbf{E} \cdot \mathbf{B}$ field. On the other hand, as we move to the $B > 0$ region, $\mathbf{E} \cdot \mathbf{B}$ turns negative, which favours state II. However, no sign of switching from state I to II is seen in the $B > 0$ region, suggesting that $\mathbf{E} \cdot \mathbf{B}$ fails to reach the coercive field $(\mathbf{E} \cdot \mathbf{B})_c$ at any point before the system goes back to the spin-flop phase at $B \approx +4$ T. This allows us to make a prediction: if we can repeat the measurement but apply a stronger electric field, then we can expect to reach the coercive field $(\mathbf{E} \cdot \mathbf{B})_c$ and hence induce a direct switching between the antiferromagnetic states I and II. Indeed, this is confirmed by the measurements shown in Fig. 4c, where direct switchings between the two antiferromagnetic states are observed. Therefore, we have demonstrated that the axion field $\mathbf{E} \cdot \mathbf{B}$ can switch between the antiferromagnetic states. This, in turn, manipulates the layer-locked Berry curvature, which is monitored by the layer Hall effect.

Such an axion field paves the way for versatile electrical manipulation of the antiferromagnetic states. In Fig. 4d, we fix the magnetic field at $B = +1$ T and scan the electric field back and forth. We observe clear hysteresis as a function of electric field, which shows a butterfly-like shape. This is because the layer-polarized AHE vanishes at $E = 0$. As such, even though a distinct antiferromagnetic state is favoured for each scan, the two scans still overlap at $E = 0$. By sweeping the electric field back and forth, repeatable switching is observed (Fig. 4e). Although our main goal here is to manipulate the layer-locked Berry curvature by the axion field $\mathbf{E} \cdot \mathbf{B}$, electrical detection and control of the magnetic order by itself is at the core of modern research in spintronics, magnetoelectrics and multiferroics^{10,11,39,40}. Achieving this in the topological axion state in MnBi_2Te_4 is of great interest (see detailed discussion in Supplementary Information section VI.7).

Discussion

Our observations suggest exciting future possibilities. First, the layer Hall effect uncovers a unique topological response of fully compensated antiferromagnetic axion insulators, which can be used to distinguish them from other systems such as the valley Hall effect or the nonlinear Hall effect in non-centrosymmetric materials, as well as the AHE in ferromagnetic materials. Second, the layer Hall effect allows us to understand how the Berry phase manifests itself in a fully compensated antiferromagnet with unique axion topology. Unlike known topological materials, the Berry curvature is found to acquire a spatial texture, paving the way for spatial engineering of Berry phase (Extended Data Fig. 1b) with exotic electromagnetism responses^{2,13,14,19,20}. Third, our demonstration of the axion field $\mathbf{E} \cdot \mathbf{B}$ manipulation of the antiferromagnetic states indicates strong magneto-electric coupling in even-layered MnBi_2Te_4 . The magneto-electric coupling in MnBi_2Te_4 is expected to be dominated by the contribution from low-energy topological electrons, leading to the novel quantized axion coupling^{12,15,16} (see Supplementary Information sections VI.5 and 6 for further discussion). Finally, the antiferromagnetic domain walls in even-layered MnBi_2Te_4 are predicted to support 1D layer-specific topological modes² (Extended Data Fig. 1a). Versatile control of the layer-locked Berry curvatures, as begun in our work, could have many applications in topological antiferromagnetic spintronics.

Online content

Any methods, additional references, Nature Research reporting summaries, source data, extended data, supplementary information, acknowledgements, peer review information; details of author contributions and competing interests; and statements of data and code availability are available at <https://doi.org/10.1038/s41586-021-03679-w>.

- Néel, L. Nobel Lecture: Magnetism and the local molecular field. *Nobel Lectures, Physics 1963–1970* (Elsevier, 1970).
- Li, X., Cao, T., Niu, Q., Shi, J. & Feng, J. Coupling the valley degree of freedom to antiferromagnetic order. *Proc. Natl Acad. Sci. USA* **110**, 3738–3742 (2013).
- Gao, Y., Yang, S. A. & Niu, Q. Field induced positional shift of Bloch electrons and its dynamical implications. *Phys. Rev. Lett.* **112**, 166601 (2014).
- Chen, H., Niu, Q. & MacDonald, A. Anomalous Hall effect arising from noncollinear antiferromagnetism. *Phys. Rev. Lett.* **112**, 017205 (2014).
- Nakatsui, S., Kiyohara, N. & Higo, T. Large anomalous Hall effect in a non-collinear antiferromagnet at room temperature. *Nature* **527**, 212–215 (2015).
- Nayak, A. K. et al. Large anomalous Hall effect driven by a nonvanishing Berry curvature in the noncollinear antiferromagnet Mn_2Ge . *Sci. Adv.* **2**, e1501870 (2016).
- Šmejkal, L., Mokrousov, Y., Yan, B. & MacDonald, A. H. Topological antiferromagnetic spintronics. *Nat. Phys.* **14**, 242–251 (2018).
- Tokura, Y., Yasuda, K. & Tsukazaki, A. Magnetic topological insulators. *Nat. Rev. Phys.* **1**, 126–143 (2019).
- Xu, Y. et al. High-throughput calculations of magnetic topological materials. *Nature* **586**, 702–707 (2020).
- Fiebig, M. Revival of the magnetoelectric effect. *J. Phys. D* **38**, R123–R152 (2005).
- Jungwirth, T., Marti, X., Wadley, P. & Wunderlich, J. Antiferromagnetic spintronics. *Nat. Nanotechnol.* **11**, 231–241 (2016).
- Essin, A. M., Moore, J. E. & Vanderbilt, D. Magnetoelectric polarizability and axion electrodynamics in crystalline insulators. *Phys. Rev. Lett.* **102**, 146805 (2009).
- Sivadas, N., Okamoto, S. & Xiao, D. Gate-controllable magneto-optic Kerr effect in layered collinear antiferromagnets. *Phys. Rev. Lett.* **117**, 267203 (2016).
- Wang, J., Lian, B. & Zhang, S.-C. Generation of spin currents by magnetic field in T - and P -broken materials. *Spin* **9**, 1940013 (2019).
- Zhang, D. et al. Topological axion states in the magnetic insulator MnBi_2Te_4 with the quantized magnetoelectric effect. *Phys. Rev. Lett.* **122**, 206401 (2019).
- Armitage, N. P. & Wu, L. On the matter of topological insulators as magnetoelectrics. *SciPost Phys.* **6**, 046 (2019).
- Šmejkal, L., González-Hernández, R., Jungwirth, T. & Sinova, J. Crystal time-reversal symmetry breaking and spontaneous Hall effect in collinear antiferromagnets. *Sci. Adv.* **6**, eaaz8809 (2020).
- Du, S. et al. Berry curvature engineering by gating two-dimensional antiferromagnets. *Phys. Rev. Res.* **2**, 022025 (2020).
- Wang, H. & Qian, X. Electrically and magnetically switchable nonlinear photocurrent in PT -symmetric magnetic topological quantum materials. *npj Comput. Mater.* **6**, 199 (2020).
- Fei, R., Song, W. & Yang, L. Giant linearly-polarized photogalvanic effect and second harmonic generation in two-dimensional axion insulators. *Phys. Rev. B* **102**, 035440 (2020).
- Li, R., Wang, J., Qi, X.-L. & Zhang, S.-C. Dynamical axion field in topological magnetic insulators. *Nat. Phys.* **6**, 284–288 (2010).
- Nagaosa, N., Sinova, J., Onoda, S., MacDonald, A. & Ong, N. P. Anomalous Hall effect. *Rev. Mod. Phys.* **82**, 1539–1592 (2010).
- Mak, K. F., McGill, K. L., Park, J. & McEuen, P. L. The valley Hall effect in MoS_2 transistors. *Science* **344**, 1489–1492 (2014).
- Otrokov, M. M. et al. Prediction and observation of an antiferromagnetic topological insulator. *Nature* **576**, 416–422 (2019).
- Rienks, E. D. L. et al. Large magnetic gap at the Dirac point in $\text{Bi}_2\text{Te}_3/\text{MnBi}_2\text{Te}_4$ heterostructures. *Nature* **576**, 423–428 (2019).
- Lee, S. H. et al. Spin scattering and noncollinear spin structure-induced intrinsic anomalous Hall effect in antiferromagnetic topological insulator MnBi_2Te_4 . *Phys. Rev. Res.* **1**, 012011 (2019).
- Yan, J.-Q. et al. Crystal growth and magnetic structure of MnBi_2Te_4 . *Phys. Rev. Mater.* **3**, 064202 (2019).
- Deng, Y. et al. Quantum anomalous Hall effect in intrinsic magnetic topological insulator MnBi_2Te_4 . *Science* **367**, 895–900 (2020).
- Liu, C. et al. Robust axion insulator and Chern insulator phases in a two-dimensional antiferromagnetic topological insulator. *Nat. Mater.* **19**, 522–527 (2020).
- Ge, J. et al. High-Chern-number and high-temperature quantum Hall effect without Landau levels. *Nat. Sci. Rev.* **7**, 1280–1287 (2020).
- Liu, C. et al. Helical Chern insulator phase with broken time-reversal symmetry in MnBi_2Te_4 . Preprint at <https://arxiv.org/abs/1910.13943> (2020).
- Deng, H. et al. High-temperature quantum anomalous Hall regime in a $\text{MnBi}_2\text{Te}_4/\text{Bi}_2\text{Te}_3$ superlattice. *Nat. Phys.* **17**, 36–42 (2021).
- Ovchinnikov, D. et al. Intertwined topological and magnetic orders in atomically thin Chern insulator MnBi_2Te_4 . *Nano Lett.* **21**, 2544–2550 (2021).
- Mogi, M. et al. Tailoring tricolor structure of magnetic topological insulator for robust axion insulator. *Sci. Adv.* **3**, eaao1669 (2017).
- Xiao, D. et al. Realization of the axion insulator state in quantum anomalous Hall sandwich heterostructures. *Phys. Rev. Lett.* **120**, 056801 (2018).
- Chang, C.-Z. et al. Experimental observation of the quantum anomalous Hall effect in a magnetic topological insulator. *Science* **340**, 167–170 (2013).
- Iyama, A. & Kimura, T. Magnetoelectric hysteresis loops in Cr_2O_3 at room temperature. *Phys. Rev. B* **87**, 180408(R) (2013).
- Jiang, S., Shan, J. & Mak, K. F. Electric-field switching of two-dimensional van der Waals magnets. *Nat. Mater.* **17**, 406–410 (2018).
- Matsukura, F., Tokura, Y. & Ohno, H. Control of magnetism by electric fields. *Nat. Nanotechnol.* **10**, 209–220 (2015).
- Tsai, H. et al. Electrical manipulation of a topological antiferromagnetic state. *Nature* **580**, 608–613 (2020).

Publisher's note Springer Nature remains neutral with regard to jurisdictional claims in published maps and institutional affiliations.

© The Author(s), under exclusive licence to Springer Nature Limited 2021

Article

Methods

Crystal growth

MnBi₂Te₄ is a newly discovered 2D van der Waals magnetic material^{24–33,41–45}. Our bulk crystals were grown by two methods (Supplementary Information section I): the Bi₂Te₃ flux method²⁷ and solid-state reaction method with extra Mn and I₂. In the Bi₂Te₃ flux method, elemental Mn, Bi and Te were mixed at a molar ratio of 15:170:270, loaded into a crucible and sealed in a quartz tube under one-third atmospheric pressure of Ar. The ampule was first heated to 900 °C for 5 h. It was then moved to another furnace where it slowly cooled from 597 °C to 587 °C and was kept for one day at 587 °C. Finally, MnBi₂Te₄ were obtained by centrifuging the ampule to separate the crystals from the Bi₂Te₃ flux. In the solid-state reaction method, elemental form of Mn, Bi, Te and I₂ were first mixed at a stoichiometric ratio of 1.5:2:4:0.5 and sealed in a quartz ampoule under vacuum. The sample was heated to 900 °C in 24 h in a box furnace and kept at the temperature for over 5 h to ensure a good mixture. The ampoule was then air quenched and moved to another furnace preheated at 597 °C, where it slowly cooled to 587 °C in 72 h and remained at the final temperature for two weeks.

Sample fabrication

To address the sensitive chemical nature of 2D MnBi₂Te₄ flakes, all fabrication processes were completed in an Ar environment without exposure to air, chemicals or heat. Specifically, the Ar-filled glovebox with O₂ and H₂O level below 0.01 ppm and a dew point below –96 °C was used. The glovebox was attached to an electron-beam evaporator, allowing us to make metal deposition without exposure to air. First, thin flakes of MnBi₂Te₄ were mechanically exfoliated from the bulk crystal onto O₂ plasma-cleaned 300-nm SiO₂/Si wafers using Scotch tape. Second, the number of layers were determined by the optical contrast of the flakes. This method has been proven effective for a wide range of air-sensitive van der Waals materials^{28,46} including MnBi₂Te₄. Specifically, the optical contrast $C = (I_{\text{flake}} - I_{\text{substrate}}) / (I_{\text{flake}} + I_{\text{substrate}})$, where I is the reflected light intensity, of MnBi₂Te₄ flakes with different thicknesses was first measured based on the optical images taken via a Nikon Eclipse LV150N microscope inside the glovebox (Extended Data Fig. 7). By extracting and averaging individual RGB values over each flake and substrate region, we obtained the optical contrast. Then the flakes were taken out of the glovebox so that the number of layers could be directly determined by atomic force microscopy. A one-to-one correspondence between the optical contrast and the number of layers was thus established. This process was repeated many times to ensure that the correspondence was reproducible and reliable (see data from different samples in Extended Data Fig. 7). For the flakes eventually selected to make devices, their thickness was determined by this optical contrast. After the transport measurements, their thickness was re-confirmed by atomic force microscopy or transmission electron microscopy (details in Supplementary Information section V.1). Third, a high-resolution stencil mask technique^{47,48} was adapted. Specifically, the device contact pattern was written onto the exposed SiN membrane via photolithography and etched via reactive ion etching. This technique yields a resolution of 1 μm. The mask was subsequently held in place with vacuum suction cups and aligned onto the MnBi₂Te₄ crystal by a microscope. Fourth, the sample/mask assembly was transferred to an e-beam evaporator for metal evaporation without exposure to air. Fifth, a 20–50-nm BN flake was transferred onto the MnBi₂Te₄ flake as the top gate dielectric. A graphite gate was transferred onto the MnBi₂Te₄/BN heterostructure.

Electrical transport measurements with dual gating

Electrical transport measurements were carried out in a physical property measurement system (PPMS, Quantum Design DynaCool). The base temperature was 1.65 K, and maximum magnetic field was 9 T. The magnetic field was applied along the out-of-plane direction. Longitudinal and Hall voltages were measured simultaneously by standard lock-in techniques. The gate voltages were applied by Keithley 2400

source meters. In such dual-gated devices, as established by previous studies^{49,50}, the charge density n and electric displacement field $D = \epsilon E$ can be controlled independently by the combination of top and bottom gate voltages V_{TG} and V_{BG} . Specifically, the charge density n can be obtained from $n = \frac{\epsilon_0 \epsilon^{\text{hBN}}}{e} (V_{\text{TG}} - V_{\text{TGO}}) / h_{\text{T}} + \frac{\epsilon_0 \epsilon^{\text{SiO}_2}}{e} (V_{\text{BG}} - V_{\text{BGO}}) / h_{\text{B}}$. The electric displacement field D can be obtained from $D = [\epsilon^{\text{SiO}_2} (V_{\text{BG}} - V_{\text{BGO}}) / h_{\text{B}} - \epsilon^{\text{hBN}} (V_{\text{TG}} - V_{\text{TGO}}) / h_{\text{T}}] / 2$. Here, $\epsilon_0 = 8.85 \times 10^{-12} \text{ F m}^{-1}$ is the vacuum permittivity; V_{TGO} and V_{BGO} correspond to the gate voltages for the resistance maximum, which is the charge neutrality with no electric field; $\epsilon^{\text{hBN}} \approx 3$ and $\epsilon^{\text{SiO}_2} \approx 3.9$ are the relative dielectric constants for hexagonal boron nitride (hBN) and SiO₂; h_{T} and h_{B} are the thicknesses of the top hBN layer and bottom SiO₂ layers. To eliminate the mixing of R_{xx} and R_{yx} signals, the R_{yx} data in the main text are antisymmetrized following conventions widely established in the community (Supplementary Information section II)²². These R_{xx} and R_{yx} data allow us to obtain the carrier mobility using two independent methods, the field effect model and Hall effect model. Both methods consistently yield a carrier mobility $\sim 1.1 \times 10^3 \text{ cm}^2 \text{ V s}^{-1}$, which is among the highest reported in MnBi₂Te₄ (refs. ^{28–33}).

First-principles calculations

First-principles band-structure calculations were performed using the projector augmented wave method as implemented in the VASP package⁵¹ within the generalized gradient approximation (GGA) schemes. Monkhorst–Pack k -point meshes ($8 \times 8 \times 4$) with an energy cut-off of 400 eV were adapted for the Brillouin zone integration of bulk MnBi₂Te₄. Experimentally determined lattice parameters were used. To treat the localized Mn 3d orbitals, we follow previous first-principles work^{24,52} on MnBi₂Te₄ and used an onsite Coulomb repulsion $U = 5.0 \text{ eV}$. The Wannier model for the bulk structure was built using the Bi p and Te p orbitals⁵³. Thin films were modelled by constructing slabs of finite thickness using bulk Wannier model parameters.

Demonstration of the layer Hall effect and excluding extrinsic origins

Extended Data Fig. 9 shows various unconventional Hall effects in quantum materials. Apart from the AHE in ferromagnets, for all other unconventional Hall effects, one would expect zero net Hall voltage because there is an equal number of electrons deflected in opposite directions. Microscopically, the opposite deflection can be understood as two copies of electrons with opposite Berry curvatures locked to an additional degree of freedom (spin, valley or layer). Because of the cancellation between opposite valleys/spins/layers, to uncover the other unconventional Hall effects, one needs to selectively probe one valley/spin/layer over the opposite. We take the example of the valley Hall effect²³. Circular light is needed to selectively probe the Berry curvature of one valley. However, the valley Hall effect is present irrespective of light.

In our experiments, electric field selectively probes one layer. With $E = 0$, our data show $\sigma^{\text{AHE}} = 0$; $E > 0$ selectively probes the bottom layer, and our data show $\sigma^{\text{AHE}} > 0$. $E < 0$ selectively probes the top layer, and our data show $\sigma^{\text{AHE}} < 0$ (assuming the electron-doped region). Therefore, our observation of the electric-field-reversible AHE shows that electrons of opposite layers deflect in opposite direction, thereby demonstrating the layer Hall effect. Crucially, the electric field is needed to uncover the layer Hall effect, but the layer Hall effect is present independent of E . Therefore, we conclude that we have observed the layer Hall effect in a fully compensated AFM with $M = 0$.

We enumerate the key essential data, including the absence of the AHE without electric field, the emergence of the AHE on application of electric field, the AHE sign-reversal with respect to electric field, its unique charge density dependence, its temperature dependence and its sharp contrast with respect to the AHE in odd-layered systems. These data are crucial for excluding various extrinsic effects. For instance, defects and inhomogeneities formed during crystal growth may cause

one particular Mn-layer to have a much stronger (or weaker) magnetization than the other Mn layers, thereby breaking the full compensation between up-spins and down-spins. This would lead to a finite magnetization and in turn a spontaneous AHE. However, the sign of the AHE in a ferromagnet is uniquely tied to the direction of the global magnetization, which cannot be significantly altered or switched by an out-of-plane electric field. Our systematic data also allow us to distinguish the layer Hall effect from the AHE in multilayered ferromagnets (for example synthetic antiferromagnets). For the multilayered ferromagnets, within a fixed magnetic state, the AHE is found to be independent of the electric field^{54,55}. By contrast, in our system, within a fixed antiferromagnetic state, the layer Hall effect is observed to change markedly with the electric field. In Supplementary Information section V.3, we present additional measurements directly probing the magnetism to demonstrate the fully compensated antiferromagnetism in our even-layered MnBi₂Te₄.

Topology and Berry phase in even-layered MnBi₂Te₄ and the \mathcal{PT} symmetry

The axion insulator is a new type of antiferromagnetic topological insulator. We can understand the formation of the axion insulator phase step by step. (1) Starting from a conventional nonmagnetic insulator, the system turns into a \mathbb{Z}_2 topological insulator with Dirac surface states by going through a band inversion. (2) Next, a particular type of antiferromagnetic order is turned on, which gaps out all surface states. The top and bottom surface states are gapped with opposite magnetization. As a result, the axion insulator features large, layer-locked Berry curvature.

The exact cancellation between the top and bottom surfaces is guaranteed by the \mathcal{PT} symmetry. Breaking \mathcal{PT} by applying an electric field causes an imbalance between the two surfaces, leading to important consequences. First, the imbalance of Berry curvature directly gives rise to the electric-field-induced Hall effect. The direction of the electric field determines which layer has a dominant contribution. Therefore, by controlling the direction of the electric field, we can selectively probe the Berry curvature from one layer over the opposite. This is our observation of the layer Hall effect. Second, the imbalance of Berry curvature also leads to the electric-field-induced magnetization (the topological magneto-electric effect).

We provide an intuitive picture: the Berry curvature serves as an effective magnetic field, under which the electron Bloch wavefunction rotates. This rotation generates an emergent magnetization. Because the top and bottom surfaces have opposite Berry curvature, they also have opposite orbital magnetization. Therefore, breaking the balance gives rise to a net magnetization. Thanks to this topological magneto-electric effect, we achieved control of the antiferromagnetic order using the axion field.

Unconventional Hall effect versus Berry curvature versus magnetization

One can study and understand unconventional Hall effects (for example, Hall effects without magnetic field) from two independent perspectives: Berry curvature and magnetization. The perspective of Berry curvature allows us to understand unconventional Hall effects in both magnetic and non-magnetic materials in a unified picture (Extended Data Fig. 9). This includes the AHE²² in ferromagnets and AHE antiferromagnets⁴⁻⁶, the spin Hall effects⁵⁶ in heavy metals, the valley Hall effect²³ and nonlinear Hall effect⁵⁷ in non-centrosymmetric materials, and the layer Hall effect in fully compensated axion insulator systems. For the AHE, one would expect a finite Hall voltage because electrons deflect towards the same direction. By contrast, for all other unconventional Hall effects, one would expect zero net Hall voltage because there is an equal number of electrons deflected in opposite directions. Microscopically, the opposite deflection can be understood as two copies of electrons with opposite Berry curvatures locked to an additional degree of freedom (spin, valley or layer). In the Berry curvature perspective, there are two contributions, the intrinsic Berry curvature contribution,

and the extrinsic skew scattering and side jump contributions. In topological systems, the Berry curvature contribution usually dominates.

On the other hand, from the perspective of magnetism, researchers have extensively discussed the relationship between AHE and magnetization. In ferromagnets, one has $\rho_H = R_0 B + R_s \mu_0 M$, where ρ_H is the Hall resistivity, μ_0 is the vacuum permeability, and R_0 and R_s are the coefficients with respect to the magnetic field B and magnetization M . On the other hand, in AHE antiferromagnets, one has $\rho_H = R_0 B + R_s \mu_0 M + \rho_H^{\text{AFM}}$ (ref. 3), where $R_0 B$ is the conventional Hall effect induced by the B field, $R_s \mu_0 M$ is the AHE induced by magnetization M , and ρ_H^{AFM} is the AHE arising from the antiferromagnetism. In Supplementary Information section V.3, we provide data to demonstrate that the electric-field induced AHE in 6SL MnBi₂Te₄ is independent of B and M . We provide some further clarifications.

First, these two perspectives are independent: whether the AHE depends on M does not determine whether the AHE arises from Berry curvature. For instance, for ferromagnetic topological materials, we have both $\sigma^{\text{AHE}} = \int_{\text{occupied states}} \Omega$ (the AHE is dominated by Berry curvature) and $\rho_H = R_s \mu_0 M$ (the AHE depends on the magnetization at $B = 0$). On the other hand, for AHE antiferromagnets⁴⁻⁶, we have $\sigma^{\text{AHE}} = \int_{\text{occupied states}} \Omega$ (the AHE is dominated by Berry curvature) and $\rho_H = R_s \mu_0 M + \rho_H^{\text{AFM}}$, $\rho_H^{\text{AFM}} \gg R_s \mu_0 M$ (the AHE is nearly independent of the magnetization at $B = 0$).

Second, the AHE cannot be treated as a direct, quantitative measurement of magnetization. For a given system, by measuring σ^{AHE} , one cannot know the magnitude of M or its absolute direction (for example, $+\hat{z}$ versus $-\hat{z}$). For example, although in ferromagnets we have $\rho_H = R_s \mu_0 M$, we cannot quantitatively measure M from ρ_H in a universal way because the coefficient R_s is not universal. R can strongly vary as one changes from one material to another. For example, ref. 58 studied two isostructural ferromagnetic Heusler compounds, Co₂VGa and Mn₂CoGa. Although they have very similar M values, Co₂VGa shows large AHE but Mn₂CoGa shows nearly zero AHE. In other words, the R_s values for Co₂VGa and Mn₂CoGa are very different although they share an identical crystal structure and have similar M values. Even within the same material, R_s is theoretically expected to depend on the charge density. For instance, the AHE is expected to vanish identically inside the bandgap of a semiconductor (without Chern number), but M does not have such a constraint. Experimentally, investigation of this requires simultaneous measurements of electrical transport and magnetization in a material where electrostatic gating is feasible. This is technically challenging and deserves future effort.

Third, while the AHE cannot be treated as a direct, quantitative measurement of magnetization M , the AHE and the M do have identical symmetry properties. Therefore, in any metallic system, the AHE and the M always appear/disappear together.

Data availability

The data that support the plots within this paper and other findings of this study are available from the corresponding authors upon reasonable request. Source data are provided with this paper.

41. Zhang, S. et al. Experimental observation of the gate-controlled reversal of the anomalous Hall effect in the intrinsic magnetic topological insulator MnBi₂Te₄. *Nano Lett.* **20**, 709–714 (2020).
42. Gordon, K. N. et al. Strongly gapped topological surface states on protected surfaces of antiferromagnetic MnBi₂Te₄ and MnBi₂Te₁₀. Preprint at <https://arxiv.org/abs/1910.13943> (2019).
43. Chen, Y. J. et al. Topological electronic structure and its temperature evolution in antiferromagnetic topological insulator MnBi₂Te₄. *Phys. Rev. X* **9**, 041040 (2019).
44. Hao, Y.-J. et al. Gapless surface Dirac cone in antiferromagnetic topological insulator MnBi₂Te₄. *Phys. Rev. X* **9**, 041038 (2019).
45. Swatek, P. et al. Gapless Dirac surface states in the antiferromagnetic topological insulator MnBi₂Te₄. *Phys. Rev. B* **101**, 161109 (2020).
46. Huang, B. et al. Layer-dependent ferromagnetism in a van der Waals crystal down to the monolayer limit. *Nature* **546**, 270–273 (2017).
47. Zhao, S. Y. F. et al. Sign reversing Hall effect in atomically thin high temperature superconductors. *Phys. Rev. Lett.* **122**, 247001 (2019).

Article

48. Deng, Y. et al. Gate-tunable room-temperature ferromagnetism in two-dimensional Fe_3GeTe_2 . *Nature* **563**, 94–99 (2018).
49. Zhang, Y. et al. Direct observation of a widely tunable bandgap in bilayer graphene. *Nature* **459**, 820–823 (2009).
50. Taychatanapat, T. & Jarillo-Herrero, P. Electronic transport in dual-gated bilayer graphene at large displacement fields. *Phys. Rev. Lett.* **105**, 166601 (2010).
51. Kresse, G. & Furthmüller, J. Efficient iterative schemes for *ab initio* total-energy calculations using a plane-wave basis set. *Phys. Rev. B* **54**, 11169–11186 (1996).
52. Otrokov, M. M. et al. Unique thickness-dependent properties of the van der Waals interlayer antiferromagnet MnBi_2Te_4 films. *Phys. Rev. Lett.* **122**, 107202 (2019).
53. Souza, I., Marzari, N. & Vanderbilt, D. Maximally localized Wannier functions for entangled energy bands. *Phys. Rev. B* **65**, 035109 (2001).
54. Newhouse-Ilige, T. et al. Voltage-controlled interlayer coupling in perpendicularly magnetized magnetic tunnel junctions. *Nat. Commun.* **8**, 15232 (2017).
55. Kanai, S. et al. Electric field-induced magnetization reversal in a perpendicular-anisotropy CoFeB-MgO magnetic tunnel junction. *Appl. Phys. Lett.* **101**, 122403 (2012).
56. Hirsch, S. Spin Hall effect. *Phys. Rev. Lett.* **83**, 1834–1837 (1999).
57. Sodemann, I. & Fu, L. Quantum nonlinear Hall effect induced by Berry curvature dipole in time-reversal invariant materials. *Phys. Rev. Lett.* **115**, 216806 (2015).
58. Manna, K. et al. From colossal to zero: controlling the anomalous Hall effect in magnetic Heusler compounds via Berry curvature design. *Phys. Rev. X* **8**, 041045 (2018).
59. Yasuda, K. et al. Stacking-engineered ferroelectricity in bilayer boron nitride. *Science* **27**, eabd3230 (2021).

Acknowledgements We thank F. Zhao and P. Kim for allowing us to use their glovebox and sample preparation facilities. We thank T. I. Andersen, G. Scuri, H. Park and M. D. Lukin for their help with magnetic measurements. We also thank F. Zhao, P. Kim, Y. Gao and C. Liu for discussions. Work in the Xu group was supported partly by the Center for the Advancement of Topological Semimetals (CATS), an Energy Frontier Research Center (EFRC) funded by the US Department of Energy (DOE) Office of Science, through the Ames Laboratory under contract DE-AC0207CH11358 (fabrication and measurements) and partly through the STC Center for Integrated Quantum Materials (CIQM), National Science Foundation (NSF) award no. ECCS-2025158 (data analysis). S.-Y.X. acknowledges the Corning Fund for Faculty Development. Q.M. acknowledges support from the CATS, an EFRC funded by the US DOE Office of Science, through the Ames Laboratory under contract DE-AC0207CH11358. C.T. acknowledges support from the Swiss National Science Foundation under project P2EZP2_191801. Y.-F.L., A. Akey, J.G., D.C.B. and L.F. were supported by the CIQM, NSF award no. ECCS-2025158. This work was performed in part at the Center for Nanoscale Systems at Harvard University, a member of the National Nanotechnology Coordinated Infrastructure Network, which is supported by the NSF under NSF award no.1541959. Work at UCLA was supported by the US DOE, Office of Science, Office of Basic Energy Sciences (BES) under award no. DE-SC0021117 for bulk sample growth, transport and magnetic property measurements. The work at Northeastern University was supported by the Air Force Office of Scientific Research under award number FA955-20-1-0322, and it benefited from the computational resources of Northeastern University's Advanced Scientific Computation Center (ASCC) and the Discovery Cluster. B.G. and A. Agarwal thank the Science Education and Research Board and the Department of Science and Technology of the government of India for financial support, and the computer centre IIT Kanpur for providing the High

Performance Computing facility. T.-R.C. was supported by the Young Scholar Fellowship Program from the Ministry of Science and Technology (MOST) in Taiwan, under a MOST grant for the Columbus Program MOST110-2636-M-006-016, the National Cheng Kung University, Taiwan, and National Center for Theoretical Sciences, Taiwan. Work at NCKU was supported by MOST, Taiwan, under grant MOST107-2627-E-006-001 and Higher Education Sprout Project, Ministry of Education to the Headquarters of University Advancement at NCKU. H.L. acknowledges support by MOST in Taiwan under grant number MOST 109-2112-M-001-014-MY3. H.-Z.L. was supported by the National Natural Science Foundation of China (11925402), Guangdong province (2016ZT06D348, 2020KCXTD001), the National Key R&D Program (2016YFA0301700), Shenzhen High-level Special Fund (G02206304, G02206404), and the Science, Technology and Innovation Commission of Shenzhen Municipality (ZDSYS20170303165926217, JCYJ20170412152620376, KYTDPT20181011104202253), and Center for Computational Science and Engineering of SUSTech. R.C. was supported by the China Postdoctoral Science Foundation (grant no. 2019M661678) and the SUSTech Presidential Postdoctoral Fellowship. C.F. was supported by the ERC Advanced Grant no. 742068 'TOPMAT' and by the Deutsche Forschungsgemeinschaft (German Research Foundation) under Germany's Excellence Strategy through Würzburg-Dresden Cluster of Excellence on Complexity and Topology in Quantum Matter—ct.qmat (EXC 2147, project-id 390858490). K.S.B. is grateful for the support of the Office of Naval Research under award no. N00014-20-1-2308. K.W. and T.T. acknowledge support from the Elemental Strategy Initiative conducted by MEXT, Japan, grant no. JPMXP0112101001 and JSPS KAKENHI grant no. JP20H00354. Z.Z., N.W., Z.H. and W.G. thank the Singapore National Research Foundation through its Competitive Research Program (CRP award no. NRF-CRP21-2018-0007, NRF-CRP22-2019-0004). X.-Y.Z., Y.-X.W. and B.B.Z. acknowledge support from NSF award no. ECCS-2041779.

Author contributions S.-Y.X. conceived the experiment and supervised the project. A.G. fabricated the devices with help from Y.-F.L., J.-X.Q., D.B., C.F., K.S.B. and Q.M. A.G. performed the transport measurements and analysed data with help from Y.-F.L., C.T., J.-X.Q., S.-C.H., D.B., T.D. and Q.M. C.H. and N.N. grew the bulk MnBi_2Te_4 single crystals. Z.Z., N.W., Z.H., W.G., J.-X.Q., C.T. and A.G. performed optical magnetic circular dichroism measurements. X.-Y.Z., Y.-X.W. and B.B.Z. performed nitrogen-vacancy centre magnetometry experiments. B.G., R.C., H.S., A. Agarwal, C.T., S.-Y.X., H.-Z.L., H.-J.T., B.S., A.B., H.L., L.F. and T.-R.C. made theoretical studies including first-principles calculations and tight-binding modelling. A. Akey, J.G. and D.C.B. performed transmission electron microscopy measurements. J.-X.Q. performed atomic force microscopy measurements. K.W. and T.T. grew the bulk hBN single crystals. S.-Y.X., A.G. and Q.M. wrote the manuscript with input from all authors. S.-Y.X. was responsible for the overall direction, planning and integration among different research units.

Competing interests The authors declare no competing interests.

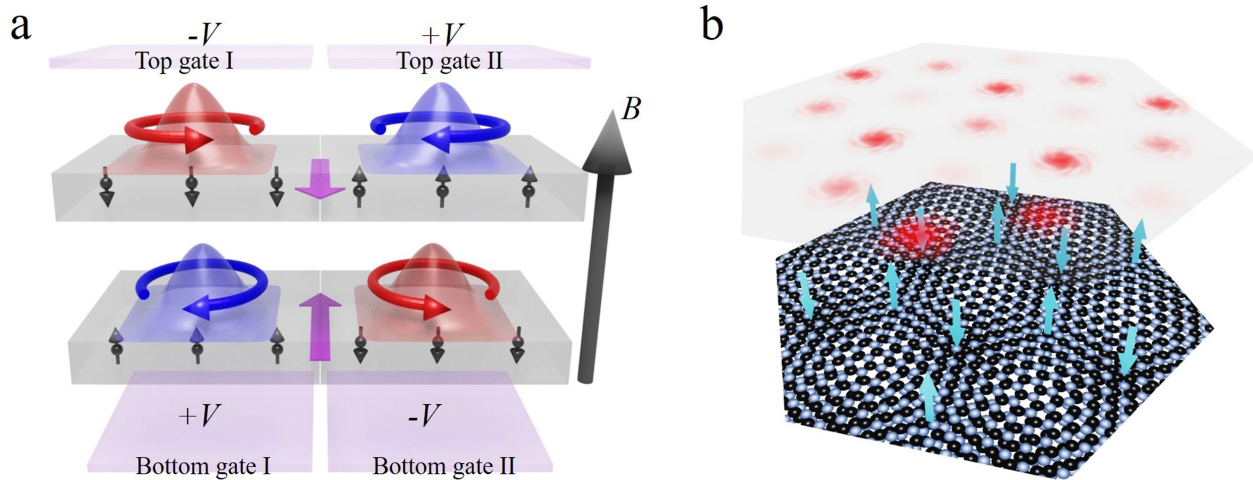
Additional information

Supplementary information The online version contains supplementary material available at <https://doi.org/10.1038/s41586-021-03679-w>.

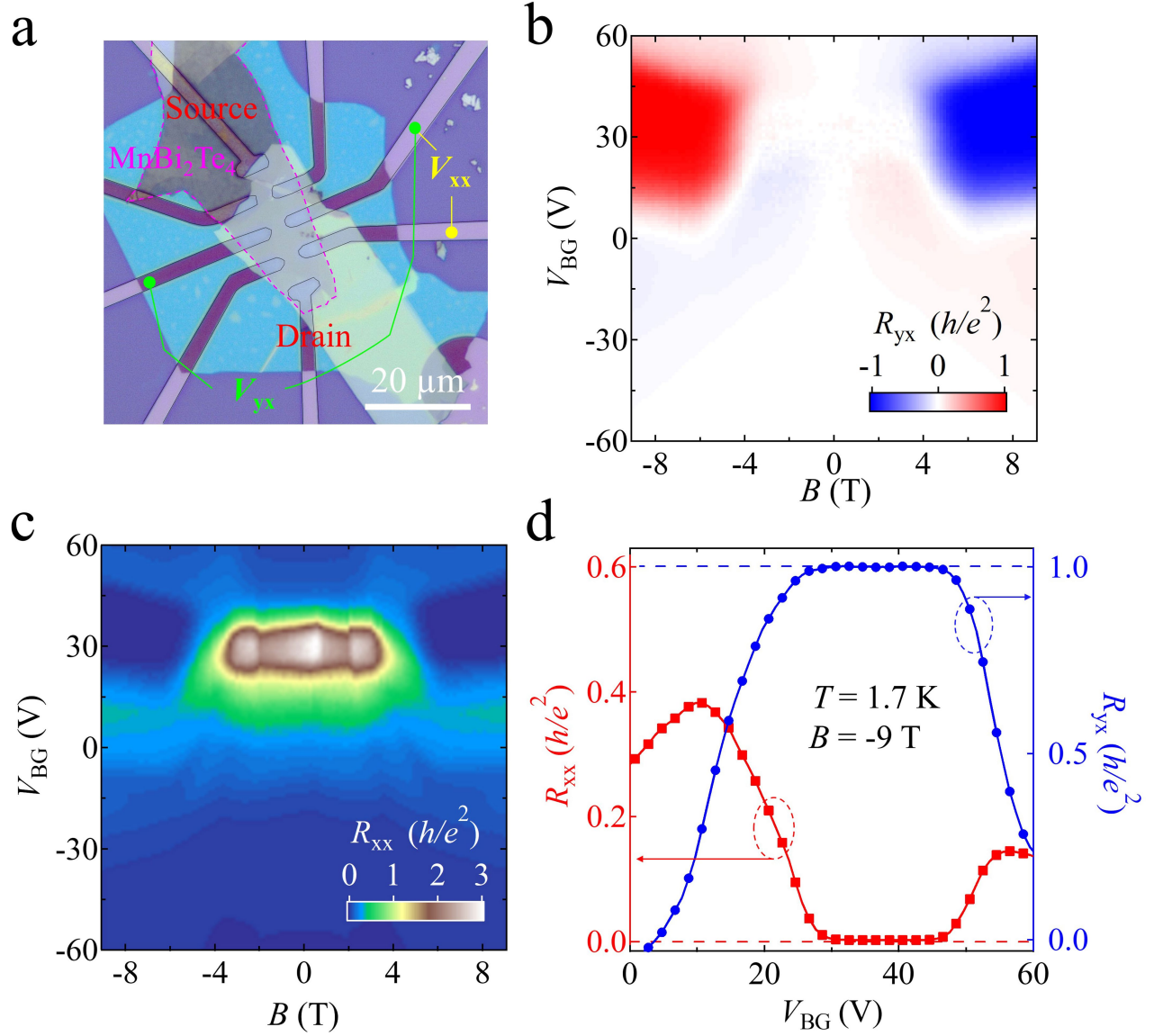
Correspondence and requests for materials should be addressed to N.N. or S.-Y.X.

Peer review information *Nature* thanks the anonymous reviewers for their contribution to the peer review of this work.

Reprints and permissions information is available at <http://www.nature.com/reprints>.



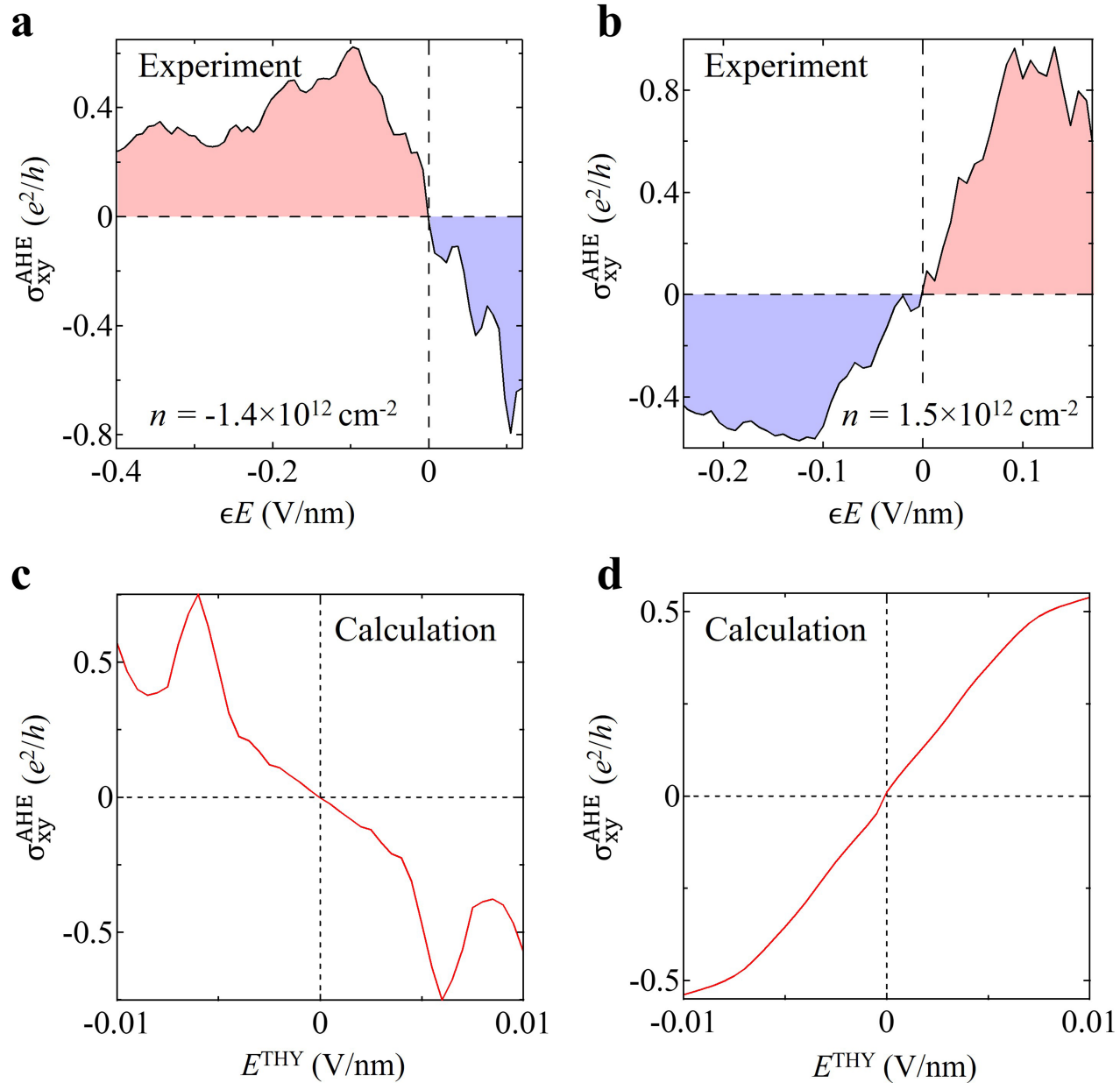
Extended Data Fig. 1 | Spatial engineering of Berry curvature. a, Topological axion domain wall constructed by the axion field $\mathbf{E} \cdot \mathbf{B}$. **b,** Spatially modulated Berry curvature moiré superlattice enabled by a MnBi_2Te_4 -twisted hBN heterostructure⁵⁹.



Extended Data Fig. 2 | Topological Chern insulator state in MnBi_2Te_4 .

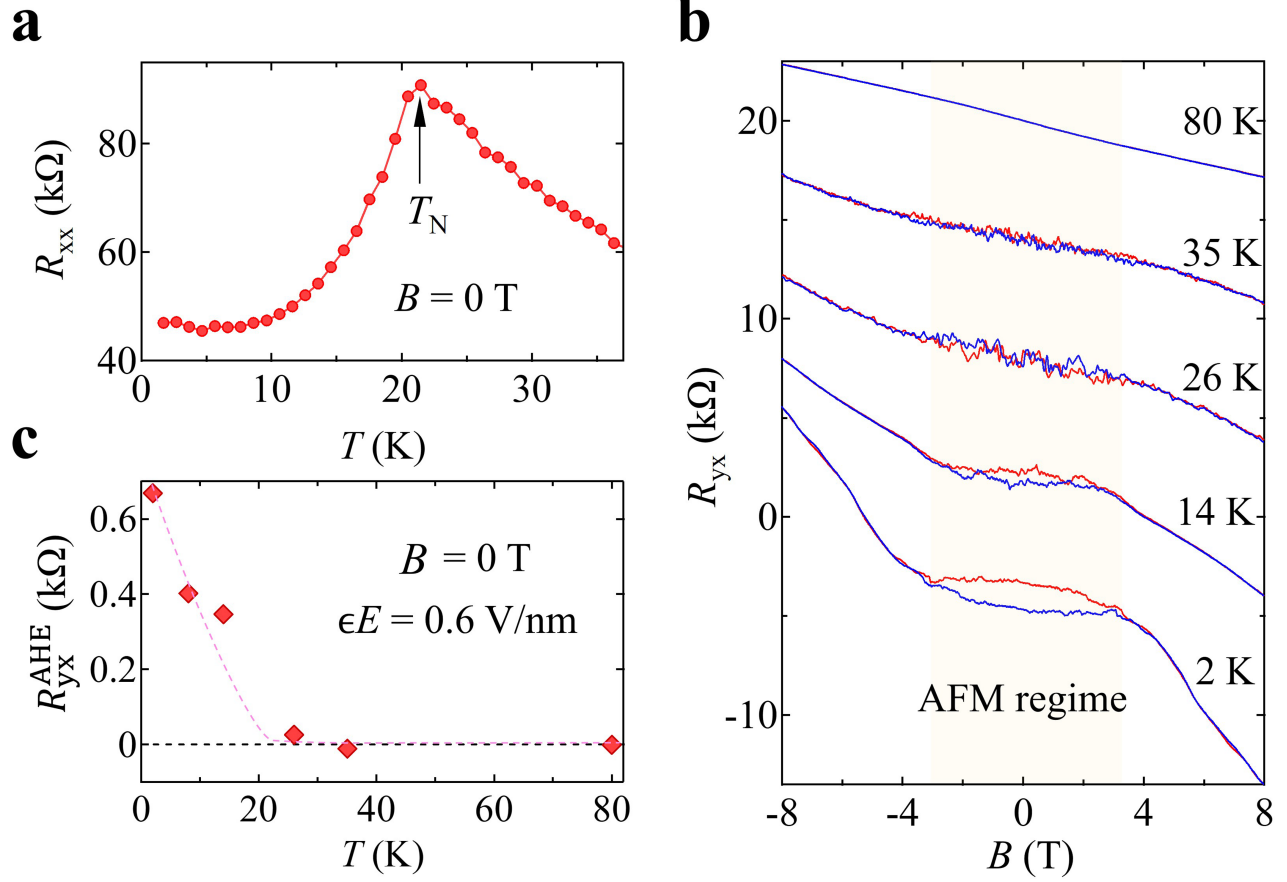
a, Microscope image of the 6SL MnBi_2Te_4 device presented in the main text. The circuit for our transport measurements is noted. **b, c**, Longitudinal R_{xx} (**c**) and

transverse (Hall) resistance R_{xy} (**b**) as a function of V_{BG} and B . **d**, R_{xx} and R_{xy} versus V_{BG} at $-9\ \text{T}$.



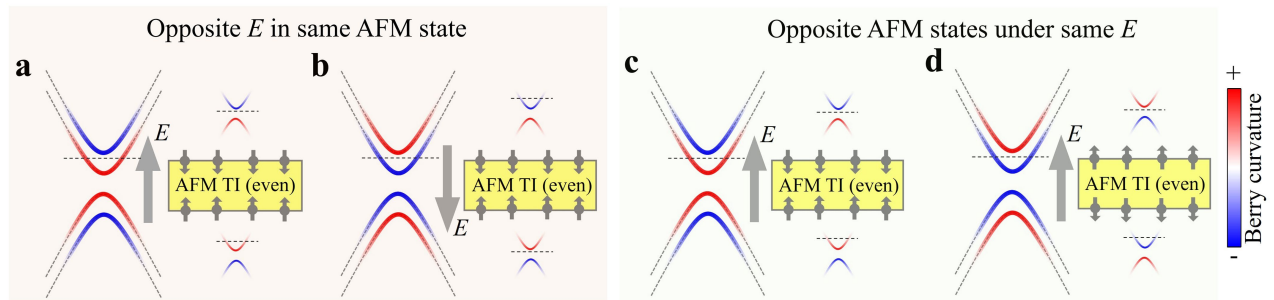
Extended Data Fig. 3 | Electric field dependence of the layer Hall effect in 6SL MnBi₂Te₄. **a**, The AHE conductivity σ_{xy}^{AHE} as a function of electric field. The charge density n is set in the hole-doped regime ($n = -1.4 \times 10^{12} \text{ cm}^{-2}$). **b**, Same as **a** but n is set in the electron-doped regime ($n = +1.5 \times 10^{12} \text{ cm}^{-2}$).

c, d, First-principles calculated AHE conductivity σ_{xy}^{AHE} as a function of electric field. **c**, Fermi level is set in the valence band (-10 meV). **d**, Fermi level is set in the conduction band ($+30 \text{ meV}$).

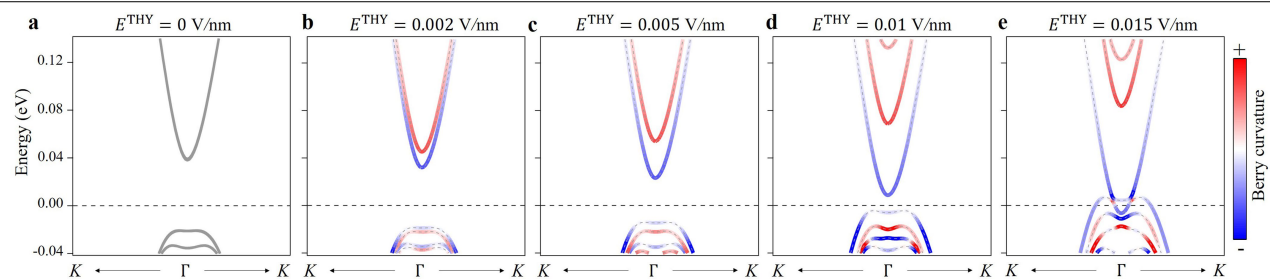


Extended Data Fig. 4 | Temperature-dependent measurements of 6SL MnBi₂Te₄. **a**, Temperature-dependent R_{xx} data showing the Néel temperature T_N . **b**, R_{xx} versus B measurements at different temperatures. Data at different

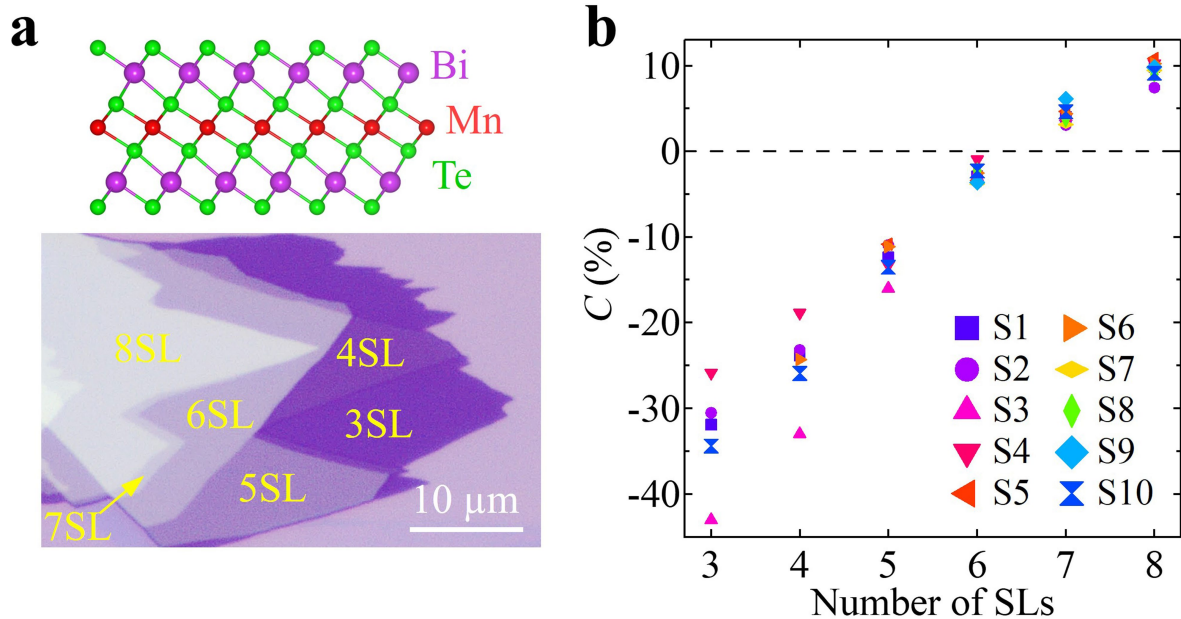
temperatures are offset by 4 k Ω for visibility at electric field 0.6 V nm⁻¹. **c**, AHE resistance as a function of temperature.



Extended Data Fig. 5 | Schematic electronic structure and Berry curvature of even-layered MnBi_2Te_4 . **a, b,** Same antiferromagnetic state under opposite electric fields. **c, d,** Opposite antiferromagnetic states under the same electric field.



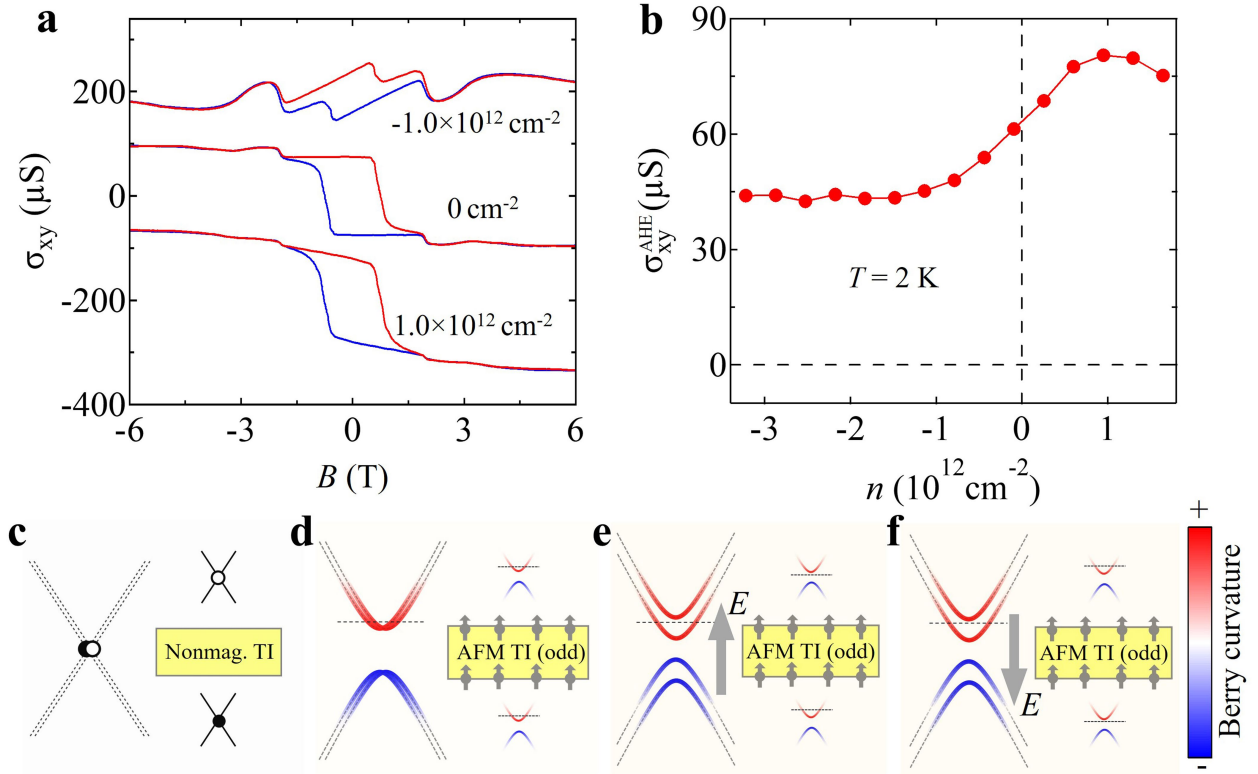
Extended Data Fig. 6 | First-principles calculated band structures. a–e, Calculated band structures of 6SL antiferromagnetic MnBi_2Te_4 for different theoretical electric fields E^{THY} .



Extended Data Fig. 7 | Optical contrast of the MnBi_2Te_4 flakes. **a.** Lower panel, optical image of few-layer flakes of MnBi_2Te_4 exfoliated on SiO_2 substrate. Upper panel, lattice of one SL MnBi_2Te_4 . **b.** Optical contrast $C = (I_{\text{flake}} - I_{\text{substrate}}) / (I_{\text{flake}} + I_{\text{substrate}})$ as a function of number of layers, which was independently determined by atomic force microscope. This process was

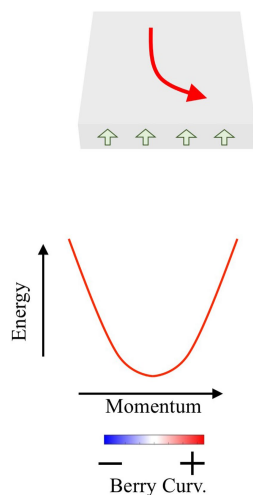
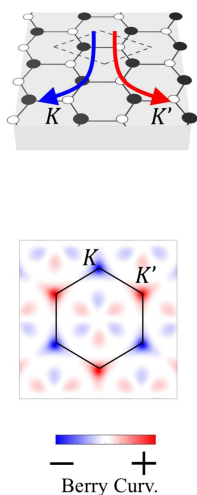
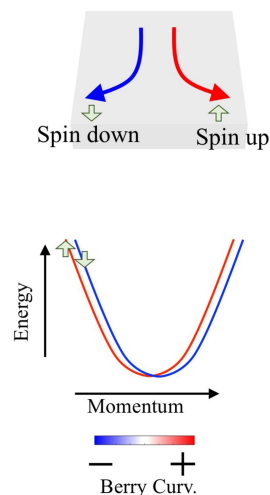
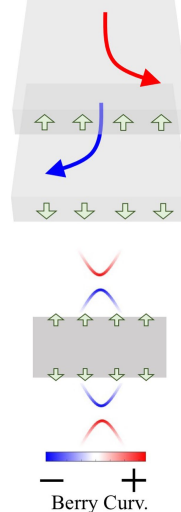
repeated on many samples (each symbol in the figure represents an independent sample) to ensure a reproducible and reliable correspondence between C and layer number (see Methods and Supplementary Information section V.1 for details).

5SL Device #1



Extended Data Fig. 8 | Experimental data and microscopic picture for odd-layered MnBi_2Te_4 . **a, b**, The AHE for 5SL MnBi_2Te_4 . In contrast to 6SL, the AHE in 5SL does not change sign as one tunes the charge density from the hole-doped regime to the electron-doped regime. Data at different n are offset by 200 μS for visibility. **c–f**, In an odd-layered antiferromagnetic system, the

top and bottom Dirac fermions experience the same magnetizations and hence open up gaps in the same fashion. As such, conduction and valence bands have the opposite Berry curvature. Therefore, the AHE remains the same sign in the hole-doped and electron-doped regimes. This conclusion is independent of E .

a Anomalous Hall effect**b** Valley Hall effect**c** Spin Hall effect**d** Layer Hall effect

Extended Data Fig. 9 | Unconventional Hall effects in a wide range of quantum materials. **a**, The AHE in ferromagnets induced by the total Berry curvature. **b**, The valley Hall effect in gapped graphene and transition metal dichalcogenides induced by the valley-locked Berry curvature. **c**, The spin Hall

effect in heavy metals induced by spin-locked Berry curvature. **d**, The layer Hall effect in the AFM axion state in even-layered MnBi_2Te_4 induced by layer-locked Berry curvature.